

***In situ* Raman analysis of sol-gel synthesised antimony particles**

Nicholas E. Drewett^{a,b}, Iain M. Aldous^a, Jianli Zou^a and Laurence J. Hardwick^{a,*}

^a Univ. Liverpool, Dept. Chem., Liverpool L69 7ZD, Merseyside, England.

^b Present address: CIC Energigune, Parque Tecnológico de Álava, Albert Einstein, Álava

* Corresponding author. Email address: Laurence.Hardwick@liverpool.ac.uk

Keywords: *in situ* Raman analyses, intermetallic antimony anode, lithium ion battery, sodium ion battery, facile sol-gel synthesis

Abstract: A one-pot sol-gel autocombustion synthesis for carbon coated antimony microparticles has been developed for the first time. The initial capacities of this material were 647 mAhg⁻¹Sb vs. Li and 527 mAhg⁻¹Sb vs. Na, with a good rate capability (8C: 398 and 356 mAhg⁻¹Sb vs. Li and Na respectively) and cyclability (cycle 120 capacity retention: 86% vs. Li, 91% vs. Na). The sol-gel synthesised Sb was found to be superior to commercial Sb of similar particle size (ca. 5 – 50 μm), which is attributed to the carbon coating. *In situ* Raman analysis was used to investigate key differences between the sol-gel synthesised and commercial antimony materials during the 1st cycle, and additionally demonstrated that upon charge both materials do not return to a crystalline material but instead to an amorphous phase represented by a broad feature centred at ca. 140 cm⁻¹.

1. Introduction

The ability to manage and store energy is crucial to modern society, and a key family of devices capable of this are alkali metal-ion batteries. Both lithium- and sodium-ion batteries are seeing increasing interest in their potential use for a wide range of areas, from transportation and portable electronic devices to both stationary and grid storage. However, with this comes an increasing demand to improve a range of properties to make them more suitable for those applications [1–6].

Intermetallic negative electrodes (anodes) have received some attention due to their potential use as high gravimetric capacity materials. However, their high gravimetric capacity is often accompanied by a large volume change during intercalation/deintercalation, which can lead to pulverisation of the particles. This in turn can result in loss of electrical contact within the anode and damage to the surface of the intermetallic particles, leading to continuous solid-electrolyte interphase (SEI) formation/breaking and irreversible capacity loss [7–10]. Nevertheless, due to their attractive properties there is still considerable appeal in developing and improving these types of materials, particularly for sodium-ion batteries [11,12].

The intermetallic anode material antimony (Sb) has a number of properties that make it of potential interest. Capable of alloying with both sodium and lithium with a theoretical gravimetric capacity of $660 \text{ mAhg}^{-1}\text{Sb}$ (based on the capacity of M_3Sb), even in its bulk form it is a reasonably attractive anode, with good reversibility at low to moderate current density [12–15]. Moreover, the use of antimony anodes offers a way to investigate and compare a wide range of lithium and sodium electrochemical systems. However, one key challenge is improving the electrochemical properties of antimony by increasing its rate capability and mitigating the stress and strain caused by volumetric changes during cycling.

One approach is to prepare new and unique micro- and nano-structures [12]. Consequently there has been interest in using antimony both as a pure anode and as a composite with other materials. Research has been carried out into the lithiation of bulk microcrystalline powders and vacuum evaporated thin-film materials [13,15], antimony/carbon nanotube composites [16] and high-energy milled or chemically synthesised antimony nanocomposites [17–21]. Stable and reversible sodiation has been demonstrated for bulk antimony and in thin films [13,15], with work also having been carried out into sodiation of antimony/carbon fibres [22] and mechanically milled antimony/carbon nanocomposites [23]. Recently, nano-sized antimony particles were synthesised and, after additional processing, were able to demonstrate excellent rate capability and cyclability during both sodiation and lithiation [14]. However, these also exhibited poorer coulombic efficiencies than bulk antimony in the initial cycle, which has attributed to the larger surface area of the nanomaterials leading to increased decomposition of electrolyte during the formation of the SEI layer [11,14].

Given that the surface stability of the antimony particles can dramatically affect the electrochemical behaviour of the resulting electrode, decorating the surface with carbon could well mitigate the effects of volume expansion and improve the cyclability of the material. One facile way to achieve this is to use a sol-gel synthetic route, as this method can often leave small traces of carbon residue on metal particles. Furthermore, since the chemistry of sol-gel syntheses has enabled the production of a wide range of materials with diverse nano- and micro-structures, some of which were used in lithium- and sodium-ion systems, a practical sol-gel route to produce antimony particles would be advantageous [24–31]. Given this, and thus the likely subsequent importance of electrochemistry occurring at surface, the use of *in situ* Raman spectroscopy presents an

opportunity to investigate and understand these processes in relation to both the carbon decorated antimony surface and the near-surface of the antimony particle itself.

However, until now few sol-gel routes have been developed for pure antimony metal particles. In part this is due to the difficulty of forming a stable sol with an antimony salt precursor, as well as the problem of controlling the oxidation, and thus combustion, of the carbon gel without oxidising the antimony metal particles. Nevertheless, by using a citric acid sol-gel route it is possible to mitigate some of these problems – the citric acid not only forms the gel, but may also be capable of chelating metal ions to form a more stable sol as well as facilitating their reduction [31–33]. Moreover, citric acid sol-gel syntheses have previously been used to make nanoparticles of other metals [34] and metal oxides, implying that should a suitable route be developed it may then be possible to control and optimise the size of the resulting particles by controlling and optimising the synthetic conditions [35,36].

In this work we report, for the first time to our knowledge, a one-pot sol-gel synthesis of pure antimony metal particles. Furthermore, we use electrochemical and *in situ* Raman spectroscopy to analyse the properties of the synthesised material, and to compare these to those of commercial antimony.

2. Experimental

2.1. Overview of sol-gel antimony synthesis

The citric acid sol-gel synthesis (Scheme 1) may be thought of as taking place over two general steps, i. Gelation and ii. Combustion.

During i. Gelation, the antimony precursor (SbCl_3) and the gelation agent (citric acid) are dissolved in ethanol, allowing the citric acid to complex with antimony ions and preventing reaction with water during the addition of small quantities of aqueous

oxidising agent (NH_4NO_3). Given that citric acid has previously been shown to be able to act as a weak reducing agent [32], it seems likely some degree of antimony reduction takes place during this stage. After heating overnight, the gel has expanded to form a white, porous, solidified foam which is then ready for combustion.

During ii. Combustion, the material is heated under an inert gas (argon). This initiates the thermal decomposition of the oxidising agent resulting in the release of, amongst others, oxygen gas, which then reacts with the hydrocarbon gel. It has previously been shown that thermal decomposition of nitrates in citric acid gels can result in the evolution of many gasses [34]. These include H_2 , H_2O , CH_4 , NO , CO_2 , NH_3 and NO_2 .

Given that H_2 and CH_4 are reducing agents it seems reasonable to conclude that some degree of antimony reduction occurs during this step. After following a suitable heating regime (as described in 2.2.), the final product was obtained. Thus, by controlling the synthetic conditions (e.g. ratio of citric acid to antimony chloride, amount of NH_4NO_3 oxidising agent, argon gas flow rate, etc.) it was possible to create the desired antimony product.

2.2. Synthesis of sol-gel antimony microparticles

Antimony trichloride (0.007 moles, 1 g) and citric acid (0.0083 moles, 1.6 g) were dissolved in ethanol (12 ml). Ammonium nitrate (0.025 moles, 2 g) was dissolved in water (2 ml). The two solutions were mixed and heated at 90 °C for approximately 0.5 hr, forming a viscous yellow gel which was then poured into a ceramic boat and heated at 95 °C for 12 hr. The resulting white porous material was then heated at 180 °C hr^{-1} under a constant argon flow (approximately 0.5 ml s^{-1}) to 200 °C for 2 hr, before being cooled and ground. It was then heated again under argon at 180 °C hr^{-1} to 640 °C for 8 hr before being cooled and ground to obtain the final product.

2.3. Coin cell fabrication and testing

Sodium and lithium electrolytes were prepared from 1 M sodium and lithium perchlorate (respectively) in dried, distilled propylene carbonate (PC), with 10 wt. % fluoroethylene carbonate (FEC) additive to improve cycling stability [13,14].

To evaluate the performance of the antimony particles, composite electrodes were fabricated by casting an aqueous mixture (antimony active material : carbon black (Super C Li, IMERYYS) : sodium carboxymethylcellulose in a ratio of 64 : 21 : 15 % by weight) onto a copper foil current collector. Coin cells were assembled from CR2025 coin cell parts, the prepared antimony electrodes, a glass fibre separator (Whatman) impregnated with the sodium or lithium electrolyte and sodium (Na) or lithium (Li) metal counter electrode. In all cases, cells were sealed in a glove box under air and moisture free conditions ($O_2 < 0.1$ ppm; $H_2O < 0.1$ ppm). The electrochemical measurements were performed at 30 °C using a Maccor Series 4000 battery cycler. All batteries were cycled in the 20 mV to 1.5 V potential range and the obtained capacities were normalised by the mass of antimony. Here the C-rate is defined for 1C as the current applied (660 Ag^{-1}) to allow full discharge or charge within 1 hour.

2.4. Other analyses

Powder X-ray diffraction patterns were collected on a PANalytical X'Pert PRO HTS X-Ray Diffractometer operating in reflection mode with $CoK\alpha_1$ radiation ($\lambda = 1.79 \text{ \AA}$).

Scanning electron microscopy images were collected on a JEOL 6610 scanning electron microscope operating at an accelerating voltage of 20.0 keV.

Raman electrodes were prepared from an electrode mixture (antimony active material : carbon black (Super C Li, IMERYYS) : poly(vinylidene fluoride-hexafluoropropylene) co-polymeric binder (Kynar-flex, Arkema) in a ratio of 40 : 22 : 38% by weight) and dibutyl phthalate (Aldrich) dispersed in acetone and cast at a thickness of 40 μm onto glass. Once dry, the free-standing film was removed from the glass plate, the dibutyl

phthalate plasticiser extracted using diethyl ether and 4 mm diameter electrodes were punched from the cast. These electrodes were then dried under vacuum at 90 °C, weighed and transferred into an argon filled glovebox (O_2 , H_2O < 1 ppm) for Raman cell assembly.

The electrode loadings were 3 mg cm^{-2} , with a typical electrode mass of $\sim 0.4 \text{ mg}$. The electrodes were then used as active material within an *in situ* Raman cell (ECC-Opto-Std, El-Cell) with 1 M $LiClO_4$ or $NaClO_4$ in PC with 10 wt.% FEC and vs. lithium or sodium metal, configured as used in previous studies in which the cell assembly is described [37–39].

All Raman spectra, both *in situ* and *ex situ*, were recorded with a Raman microscope (Renishaw inVia) using a 633 nm wavelength laser focussed through a microscope (Leica) via a 50x objective (Leica).

3. Results and discussion

3.1. Material characterisation

In Figure 1 A) the powder X-ray diffraction (PXRD) pattern of the sol-gel synthesised antimony is compared to those of a commercial antimony (Fisher Scientific, antimony powder ~ 200 mesh) and a ICSD (Inorganic Crystal Structure Database) standard (PDF number: 01-073-7856). There is a good agreement between the three powder XRD patterns, demonstrating that the bulk of the sol-gel antimony has no antimony oxide impurity.

Figure 1 B) shows the scanning electron microscope (SEM) images of the sol-gel synthesised and commercial antimony. From this it can be seen that both materials consist of particles with a broadly similar size range ($\sim 5 - 50 \mu\text{m}$). However, though there are similarities between the two materials in terms of the morphology (i.e. large-

to-small particles) and broad particle size range, the commercial material appears to have a more ‘corrugated’ surface in comparison to the sol-gel antimony (likely due to the choice of synthetic route). The sol-gel material, by comparison, appears to consist of particles with a smoother surface, likely partly due to the antimony salt being well dispersed throughout the sol-gel and partly due to carbon coating. Nevertheless, the similar size range and similar morphology enables comparison between the two materials.

The Raman spectra of the two materials were taken, as shown in Figure 1 C). While both materials showed the expected antimony E_g and A_{1g} bands, only the sol-gel synthesised antimony exhibited a signal attributable to the D and G modes of disordered carbon. It should also be noted that it is possible to observe differences in the positions of the sol-gel and commercial antimony A_{1g} and E_g bands (sol-gel: 145 and 114 cm^{-1} ; commercial: 143 and 109 cm^{-1} , respectively). It is possible to attribute these shifts to confinement and strain resulting from the carbon coating of the particles [40], while the shift in E_g band may also be related to increased background fluorescence from surface groups upon the carbon coating. The Raman spectra of the sol-gel antimony, taken from multiple particles throughout the sample, showed only bands attributable to Sb and carbon. The ratios of peak intensities were similar at all points, implying a relatively high degree of homogeneity at the 1 μm scale (i.e. the limit of resolution determined by the area of the Raman laser).

In order to determine the amount of carbon present in both the sol-gel and commercial antimony materials, carbon, hydrogen and nitrogen were quantified using CHN analyses (see supplementary information, Table A1). Comparison between sol-gel and commercial Sb revealed a greater quantity of all three elements, but particularly carbon, for the sol-gel synthesised material (23.3 vs. 0.5 wt. % C for the sol-gel and commercial

antimony materials respectively). This is perhaps unsurprising given that sol-gel methods, particularly when undertaken under an inert gas, have previously been shown to be able to decorate or coat synthesised materials in a carbon layer, often leading to improved electrochemical performance [41–43].

3.2. Cyclability and rate capability

To investigate the electrochemistry of the sol-gel and commercial antimony materials, coin cell electrodes were fabricated and cycled at either $C/2$ or varying C rates to produce the plots shown in Figure 2. Plots of cell potential vs. capacity were then extracted for both the sol-gel synthesised and the commercial antimony vs. Li and vs. Na, as seen in in Figure 3.

From Figure 2 A) and C) it can be seen that vs. Na and Li the cyclability of the sol-gel synthesised antimony (Cycle 120 capacity retention: 86% vs. Li, 91% vs. Na) is superior to that of the commercial antimony (Cycle 120 capacity retention: 45% vs. Li, 16% vs. Na). Given that appropriate carbon coating can help mitigate the performance loss resulting from the cycling-induced antimony volume changes [17,44], it seems likely that the disordered carbon coating layer seen in the Raman spectrum is responsible for the superior performance of sol-gel synthesised antimony. The improvement in cyclability is even more noticeable vs. Na than vs. Li, and may be a result of the differences in expected volume changes [15] ($\sim 293\%$ vs. Na, $\sim 135\%$ vs. Li) causing greater pulverisation of the commercial antimony due to the absence of surface protection comparative to the carbon coated sol-gel antimony.

The initial capacity vs. Li for the sol-gel antimony ($647 \text{ mAhg}^{-1}\text{Sb}$) is close to the theoretical capacity of antimony (ca. 660 mAhg^{-1}), and is higher than that of the commercial antimony ($622 \text{ mAhg}^{-1}\text{Sb}$), which is also likely due to the enhanced surface stability produced through the sol-gel route. The capacities of the initial cycles vs. Na

are higher for the commercial antimony ($582 \text{ mAhg}^{-1}\text{Sb}$) than for the sol-gel synthesised antimony ($527 \text{ mAhg}^{-1}\text{Sb}$). This has been previously observed in other studies into carbon coated antimony [45–47], and may be a result of decreased diffusion of the larger sodium-ions through the carbon decorated interface.

Due to the differences in cyclability, it is impossible to directly compare the rate capabilities of the sol-gel synthesised and commercial antimony materials. Nevertheless, by comparing the 8C (cycles 42 – 51) and C/2 data (cycles 52 – 50) from Figure 2 B) and D), it can be seen that the sol-gel material exhibits good rate capability vs. both Li (at 8C: $398 \text{ mAhg}^{-1}\text{Sb}$, 70% retention) and Na (at 8C: $356 \text{ mAhg}^{-1}\text{Sb}$, 72% retention). This is in contrast to the commercial vs. Li (at 8C: $285 \text{ mAhg}^{-1}\text{Sb}$, 61% retention) but particularly vs. Na (at 8C: $48 \text{ mAhg}^{-1}\text{Sb}$, 35% retention).

Examination of the load curves of the antimony materials (Figure 3) reveals some differences. For both vs. Li and vs. Na the first cycle discharge of the sol-gel synthesised antimony plateaus at a lower voltage ($\sim 0.7 \text{ V}$ vs. Li^+/Li , $\sim 0.4 \text{ V}$ vs. Na^+/Na) than that of the commercial antimony ($\sim 0.86 \text{ V}$ vs. Li^+/Li , $\sim 0.55 \text{ V}$ vs. Na^+/Na) and those generally reported in the literature. Nevertheless, from the first cycle charge the sol-gel synthesised antimony does exhibit plateaus at the same voltages as those in the commercial antimony, implying similar alloying mechanisms in both.

The lithiation of antimony is believed to proceed via one intermediary crystalline phase (Li_2Sb), giving rise to two plateaus which are generally indistinguishable and occur below 0.9 V vs. Li^+/Li [14,48,49]. Delithiation then proceeds directly from Li_3Sb to Sb, giving one plateau at $\sim 1 \text{ V}$ vs. Li^+/Li . This is in keeping with the observed results for the commercial antimony and the sol-gel synthesised antimony after the first lithiation. From the irreversible capacity data on cycling vs. lithium (see supplementary information, Table A2) it can be seen that although the first cycle irreversible capacity

of the sol-gel synthesised antimony is larger than that of the commercial antimony, on subsequent cycles it is less. This would suggest that not all the capacity below 0.35 V vs. Li^+/Li is irreversible. Moreover, this lower irreversible capacity would support the proposal that the sol-gel antimony is benefiting from some degree of enhanced surface stability.

The sodiation mechanism is more complex, involving multiple crystalline and amorphous phases. Furthermore, the 1st cycle sodiation mechanism differs from that of subsequent cycles, giving rise to one observable plateau at ~ 0.5 V vs. Na^+/Na on discharge for the 1st cycle and two observable plateaus at ~ 0.75 V vs. Na^+/Na and ~ 0.5 V vs. Na^+/Na thereafter. Consequently, assignment of the exact electrochemical processes occurring at any given point is challenging, though studies for thin film [50] and bulk antimony [51] do exist which help to explain these mechanisms. After the first sodiation of the sol-gel synthesised antimony, on desodiation a flat plateau at ~ 0.75 V vs. Na^+/Na and a sloping plateau at $\sim 0.8 - 0.9$ V vs. Na^+/Na is observed. On subsequent sodiations, plateaus are observed starting at ~ 0.7 V, ~ 0.55 V and ~ 0.47 V vs. Na^+/Na . These results are comparable to the commercial antimony, and are in keeping with the literature. Examination of the irreversible capacity data on cycling vs. sodium (see supplementary information, Table A3) shows less irreversible capacity for the sol-gel synthesised antimony from cycles 1 to 10, which would be in keeping with what would be expected for a material with enhanced surface stability. Although the sol-gel antimony has slightly greater irreversible capacity than the commercial antimony for cycles 60 and 120, that may be a facet of the former's far greater charge and discharge capacity.

Examination of the load curves shown in Figure 3 also reveals that the sol-gel antimony exhibits greater capacity below 0.35 V than the commercial antimony. Given

the lower irreversible capacity of the sol-gel antimony, it is unlikely that this is SEI formation. Furthermore, a similar phenomenon has been observed for other carbon-coated antimony materials [45–47], which indicates it is again a result of the carbon coating.

3.3. *In situ* Raman spectroscopy

To further explore the electrochemical processes undergone by the materials, *in situ* Raman studies were carried out on the prepared Raman electrodes of both sol-gel synthesised and commercial antimony vs. Li and vs. Na. Raman cells were assembled as shown in Figure 4, which were then cycled at a slow rate of 66 mAg⁻¹Sb (C/10). It should be noted that, due to the requirements for a free standing electrode for *in situ* Raman analysis, the electrode formulation not optimised for long term cycling. The higher carbon fraction and PVDF based binder is less flexible for volume expansion, leading to a greater overpotential which is due to higher internal resistance.

There is also noticeably greater SEI formation (2 to 1.5 V vs. Li⁺/Li, 1.2 to 0.75 V vs. Na⁺/Na) which is attributed to the reaction of FEC with the greater electrode fraction of carbon black (approximate ratios Sb : C, Raman cast 3 : 1, coin cell cast 2 : 1).

In situ Raman spectroscopy was carried out on the sol-gel synthesised antimony vs. Li, as shown in Figure 5. It has previously been shown that the structure at OCP is trigonal A7 [52]. The A7 lattice system is rhombohedral and contains six atoms in the unit cell occupying 6c position, denoted as the Sb-I phase. This is seen spectroscopically as the A_{1g} and E_g bands (at 150 cm⁻¹ and 112 cm⁻¹ respectively), which correspond to longitudinal and transverse motion within the structure respectively [52].

During lithiation there is no noticeable change in the Raman spectra until ~0.9 V vs. Li⁺/Li, indicating that this phase is stable up till then. At this point there is an observable decrease in the A_{1g} and E_g bands as the long range features in the antimony are lost. This

continues until 0.02 V vs. Li^+/Li , at which point there no A_{1g} or E_g bands are visible. Interestingly, the A_{1g} band intensity decreases faster than the E_g band, implying lithiation affects the longitudinal order more rapidly.

On delithiation to 1.5 V vs. Li^+/Li the A_{1g} band at 152 cm^{-1} re-emerges, suggesting that some degree of long range ordering is returning to the antimony system on delithiation.

The sol-gel synthesised antimony does show some differences in comparison to the *in situ* Raman of the commercial antimony, shown in Figure A1. While the commercial antimony does exhibit a noticeable decrease of the A_{1g} band, there is little change during the plateau. Afterwards the A_{1g} band continues decreasing until $\sim 0.2\text{ V}$ vs. Li^+/Li , whereupon a decrease in the E_g band is also observed. However, unlike the sol-gel antimony, even when held at 0.02 V vs. Li^+/Li it is still possible to observe the A_{1g} and E_g bands, indicating some degree of long range order is retained. On delithiation there is little change to those A_{1g} and E_g bands. This is due to some antimony particles becoming electronically disconnected during Li^+ insertion and extraction as volume expansion occurs. The carbon coating can be attributed to maintaining improved electronic contact during ion insertion.

When cycled vs. Na it is possible to observe changes in the Raman spectral series of the sol-gel synthesised antimony, shown in Figure 6, corresponding to structural changes within the material. During cell discharge no peak shift is observed, suggesting this phase is stable until 0.59 V vs. Na^+/Na , where the intensity of both peaks decreases and diminishes. This is expected for an alloying mechanism between sodium and antimony [51].

Upon sodiation below 0.59 V vs. Na^+/Na , it is possible to observe diminishing long range features for antimony. Here that is seen below 0.44 V vs. Na^+/Na as the E_g band

disappears into the noise [51,52]. The weak presence of the A_{1g} band shows that some order remains within the structure [52]. This is most likely similar to the recently proposed phase of undersodiated Na_3Sb or $a-Na_{3-x}Sb$ upon the initial sodiation of the antimony structure [51].

This contrasts with the commercial antimony (see supplementary information, Figure A2), where the complete fade of the A_{1g} band suggests that complete sodiation has taken place, forming the Na_3Sb product. This could result from the carbon coating restricting sodium access to the sol-gel synthesised antimony. It may be that the carbon coating is hindering the diffusion of the larger sodium ions into the antimony particles, which would also explain the reduction in capacity compared to commercial antimony. The presence of a broad band at $\sim 187\text{ cm}^{-1}$, seen in both the commercial and sol-gel synthesised antimony samples below 0.35 V vs. Na^+/Na , may be attributable to a weak signal from a $NaSb$ phase [53]. The appearance of a broad feature at $\sim 165\text{ cm}^{-1}$, also seen in both materials, is indicative of host guest structures formed with the inclusion of sodium atoms. These type of structures have previously been characterised from Raman data of antimony, under pressure, as incommensurate monoclinic and tetragonal host guest phases [52].

Upon charge, both the sol-gel synthesised and commercial antimony structures do not return to a crystalline material, but instead to amorphous phases, represented by a broad feature in the Raman spectra centred at ca. 140 cm^{-1} (spectrum 14 in Figure 5, 6, A1 and A2). The appearance of a third feature (Figure 6, spectrum 14, 2.0 V) at $\sim 160\text{ cm}^{-1}$ suggests that a partial host guest structure has remained, with Na^+ trapped within the antimony host.

To investigate the effect of discharge/charge on the carbon present in the sol-gel synthesised material, Raman spectra were taken both vs. Li and vs. Na as shown in

Figure A3 A) and B). From this it can be seen that, during lithiation, there is a noticeable shift in the G band from higher to lower wavenumbers (from ca. 1593 to 1543 cm^{-1}), as well as a considerable decrease in the intensity of the D and G bands. This is in keeping with previous observations regarding the lithiation of amorphous carbons [54]. Hence, some degree of Li^+ insertion is occurring not only in the sol-gel synthesised antimony, but also in the accompanying carbon coating. During sodiation there also appears to be a slight decrease in D and G band intensity, though not to the same extent as during lithiation. Thus the carbon coating was found to not sodiate to the same degree as it lithiates. Similar to the delithiation, the desodiation does not appear to be completely reversible.

The difference in the degree of lithiation of the sol-gel synthesised antimony carbon, comparative to sodiation, may also be a contributing factor to the observed differences between the capacity of the sol-gel synthesised material when cycled vs. Li and vs. Na, with the carbon contributing to some of the larger capacity when cycled vs. Li. Given that we propose the carbon is also improving the cyclability of the sol-gel synthesised antimony this may mean that a more optimised synthesis, designed to leave only the minimum carbon necessary to improve performance, could result in a material with both greater cyclability and gravimetric capacity vs. Na.

From the examination of the electrochemistry and *in situ* Raman spectra of sol-gel synthesised and commercial antimony materials, some observations may be highlighted:

The sol-gel synthesised antimony exhibits cyclability superior to that of the commercial material, likely due to the former's carbon coating protecting against surface damage and the creation of electronically disconnected and inactive particles, resulting from volume changes on cycling.

On the 1st cycle, the load curves show that the sol-gel antimony plateaus at a lower voltage than the commercial. This may be attributed to increased internal resistance resulting from the carbon coating.

The *in situ* Raman spectra of the sol-gel synthesised antimony exhibit some differences to those of the commercial antimony during lithiation and sodation. The A_{1g} and E_g bands of the sol-gel antimony completely disappear indicating the loss of long range order. By contrast, in the commercial material these bands were still visible highlighting formation of electronic disconnected regions within the composite electrode. The *in situ* Raman spectra during sodiation are also of interest, showing that the sol-gel synthesised antimony does not appear to fully sodiate. It is proposed that the carbon coating restricts access for the larger sodium ions, reducing their ability to diffuse into the antimony particles.

Additionally, examination of the *in situ* Raman spectra of the D and G bands assigned to the carbon coating of the sol-gel synthesised antimony demonstrates variation in the behaviour vs. Li and Na. It is likely that the carbon coating is able to reversibly (de)lithiate to a slightly greater extent than it is able to (de)sodiate. Thus it may be that the carbon coating is able to contribute to some degree to the capacity of the material, and to do more so vs. Li than vs. Na.

These insights, provided by the *in situ* Raman data, would explain why the sol-gel antimony exhibits a slightly better capacity than the commercial when cycled vs. Li, but an initially worse capacity when cycled vs. Na.

Finally, it is worth noting that the cyclability and rate capability of the sol-gel material is superior to that of the commercial material, and compares favourably to recent literature reports [45–47], demonstrating the utility of this particular synthetic route.

4. Conclusions

In summary, a general sol-gel synthetic route to antimony particles has been developed. Even without any attempts to further optimise size or morphology this has resulted in the formation of particles of dimensions 5 – 50 μm .

The synthesised sol-gel antimony has exhibited good electrochemical performance for a material with particles of this size (647 and 622 $\text{mAhg}^{-1}\text{Sb}$ vs. Li and Na respectively), when compared to both the commercial material (582 and 527 $\text{mAhg}^{-1}\text{Sb}$ vs. Li and Na respectively). It also demonstrated decent rate capability (at 8C: 398 and 356 $\text{mAhg}^{-1}\text{Sb}$ vs. Li and Na respectively; 70% and 72% retention at C/2) and cyclability (Cycle 120 capacity retention: 86% vs. Li, 91% vs. Na).

While these initial results for sol-gel synthesised antimony are promising for battery anodes, further work is necessary and should be carried out into investigating and optimising parameters in order to improve the materials electrochemical properties (e.g. through the use of capping agents, different antimony precursors, any form of ball milling / sieving or using different synthetic parameters such as different antimony precursors or gelation times). However, we have demonstrated that it should now be possible to exploit the tailorable nature of sol-gel synthetic routes to produce a wider particle size range of antimony materials than previously accessible. Thus we believe this work represents an important first step towards the wider use of antimony in future battery electrochemical studies.

Finally, the use of *in situ* Raman to explore the 1st cycle charge and discharge vs. Na and Li has revealed key differences between the sol-gel and commercial antimony materials, which were then examined with respect to electrochemical behaviour. This has demonstrated the utility of *in situ* Raman as a complementary analytical technique for investigating alloying anode materials.

5. Acknowledgements

We acknowledge the Engineering and Physical Sciences Research Council (EPSRC) for the funding of this research under grant number EP/K016954, and the Nanoinvestigation Centre at Liverpool (NiCaL) for access to SEM instrumentation.

6. References

- [1] K. C. Divya, J. Østergaard, Battery energy storage technology for power systems—An overview, *Electr. Power Syst. Res.* 79 (2009) 511.
- [2] B. Scrosati, J. Garche, Lithium batteries: Status, prospects and future, *J. Power Sources.* 195 (2010) 2419.
- [3] P. G. Bruce, S. A. Freunberger, L. J. Hardwick, J.-M. Tarascon, Li-O₂ and Li-S batteries with high energy storage, *Nat. Mater.* 11 (2012) 19.
- [4] L. Lu, X. Han, J. Li, J. Hua, M. Ouyang, A review on the key issues for lithium-ion battery management in electric vehicles, *J. Power Sources.* 226 (2013) 272.
- [5] J. B. Goodenough, K.-S. Park, The Li-Ion Rechargeable Battery: A Perspective, *J. Am. Chem. Soc.* 135 (2013) 1167.
- [6] K. Kubota, S. Komaba, Review—Practical Issues and Future Perspective for Na-Ion Batteries, *J. Electrochem. Soc.* 162 (2015) A2538.
- [7] M. Holzapfel, H. Buqa, L. J. Hardwick, M. Hahn, A. Würsig, W. Scheifele, P. Novák, R. Kötz, C. Veit, F.-M. Petrat, Nano silicon for lithium-ion batteries, *Electrochim. Acta.* 52 (2006) 973.

- [8] M. Marcinek, L. J. Hardwick, T. J. Richardson, X. Song, R. Kostecki, Microwave plasma chemical vapor deposition of nano-structured Sn/C composite thin-film anodes for Li-ion batteries, *J. Power Sources*. 173 (2007) 965.
- [9] C. M. Hayner, X. Zhao, H. H. Kung, *Materials for Rechargeable Lithium-Ion Batteries*, *Annu. Rev. Chem. Biomol. Eng.* 3 (2012) 445.
- [10] H. Tian, F. Xin, X. Wang, W. He, W. Han, High capacity group-IV elements (Si, Ge, Sn) based anodes for lithium-ion batteries, *J. Mater.* 1 (2015) 153.
- [11] Y. Kim, K.-H. Ha, S. M. Oh, K. T. Lee, High-Capacity Anode Materials for Sodium-Ion Batteries, *Chem. Eur. J.* 20 (2014) 11980.
- [12] H. Kang, Y. Liu, K. Cao, Y. Zhao, L. Jiao, Y. Wang, H. Yuan, Update on anode materials for Na-ion batteries, *J. Mater. Chem. A*. 3 (2015) 17899.
- [13] A. Darwiche, C. Marino, M. T. Sougrati, B. Fraise, L. Stievano, L. Monconduit, Better Cycling Performances of Bulk Sb in Na-Ion Batteries Compared to Li-Ion Systems: An Unexpected Electrochemical Mechanism, *J. Am. Chem. Soc.* 134 (2012) 20805.
- [14] M. He, K. Kravchyk, M. Walter, M. V Kovalenko, Monodisperse Antimony Nanocrystals for High-Rate Li-ion and Na-ion Battery Anodes: Nano versus Bulk, *Nano Lett.* 14 (2014) 1255.
- [15] L. Baggetto, P. Ganesh, C.-N. Sun, R. A. Meisner, T. A. Zawodzinski, G. M. Veith, Intrinsic thermodynamic and kinetic properties of Sb electrodes for Li-ion and Na-ion batteries: experiment and theory, *J. Mater. Chem. A*. 1 (2013) 7985.
- [16] W. X. Chen, J. Y. Lee, Z. Liu, The nanocomposites of carbon nanotube with Sb and

- SnSb_{0.5} as Li-ion battery anodes, Carbon N. Y. 41 (2003) 959.
- [17] C.-M. Park, S. Yoon, S.-I. Lee, J.-H. Kim, J.-H. Jung, H.-J. Sohn, High-Rate Capability and Enhanced Cyclability of Antimony-Based Composites for Lithium Rechargeable Batteries, J. Electrochem. Soc. 154 (2007) A917.
- [18] Á. Caballero, J. Morales, L. Sánchez, A simple route to high performance nanometric metallic materials for Li-ion batteries involving the use of cellulose: The case of Sb, J. Power Sources. 175 (2008) 553.
- [19] C.-M. Park, H.-J. Sohn, Novel Antimony/Aluminum/Carbon Nanocomposite for High-Performance Rechargeable Lithium Batteries, Chem. Mater. 20 (2008) 3169.
- [20] J. H. Sung, C.-M. Park, Amorphized Sb-based composite for high-performance Li-ion battery anodes, J. Electroanal. Chem. 700 (2013) 12.
- [21] Y. Cheng, Z. Yi, C. Wang, L. Wang, Y. Wu, L. Wang, Nanostructured Carbon/Antimony Composites as Anode Materials for Lithium-Ion Batteries with Long Life, Chem. Asian J. 11 (2016) 2173.
- [22] Y. Zhu, X. Han, Y. Xu, Y. Liu, S. Zheng, K. Xu, L. Hu, C. Wang, Electrospun Sb/C Fibers for a Stable and Fast Sodium-Ion Battery Anode, ACS Nano. 7 (2013) 6378.
- [23] J. Qian, Y. Chen, L. Wu, Y. Cao, X. Ai, H. Yang, High capacity Na-storage and superior cyclability of nanocomposite Sb/C anode for Na-ion batteries, Chem. Commun. 48 (2012) 7070.
- [24] H. Liu, Y. P. Wu, E. Rahm, R. Holze, H. Q. Wu, Cathode materials for lithium ion batteries prepared by sol-gel methods, J. Solid State Electrochem. 8 (2004) 450.

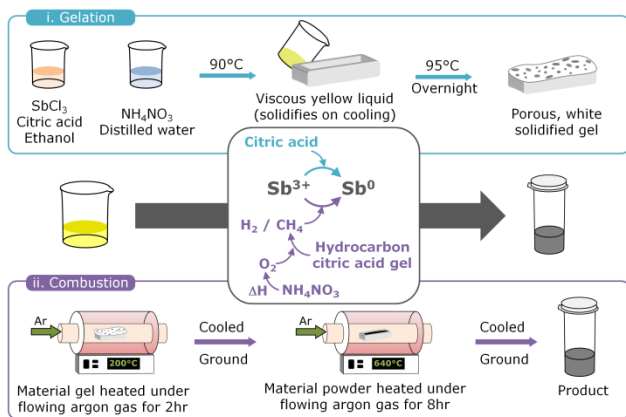
- [25] L. J. Fu, H. Liu, C. Li, Y. P. Wu, E. Rahm, R. Holze, H. Q. Wu, Electrode materials for lithium secondary batteries prepared by sol–gel methods, *Prog. Mater. Sci.* 50 (2005) 881.
- [26] K. Dokko, J. Sugaya, H. Nakano, T. Yasukawa, T. Matsue, K. Kanamura, Sol–gel fabrication of lithium-ion microarray battery, *Electrochem. Commun.* 9 (2007) 857.
- [27] D. Yuan, W. He, F. Pei, F. Wu, Y. Wu, J. Qian, Y. Cao, X. Ai, H. Yang, Synthesis and electrochemical behaviors of layered $\text{Na}_{0.67}[\text{Mn}_{0.65}\text{Co}_{0.2}\text{Ni}_{0.15}]\text{O}_2$ microflakes as a stable cathode material for sodium-ion batteries, *J. Mater. Chem. A.* 1 (2013) 3895.
- [28] M. Iftexhar, N. E. Drewett, a. R. Armstrong, D. Hesp, F. Braga, S. Ahmed, L. J. Hardwick, Characterization of Aluminum Doped Lithium-Manganese Rich Composites for Higher Rate Lithium-Ion Cathodes, *J. Electrochem. Soc.* 161 (2014) A2109. <http://jes.ecsdl.org/cgi/doi/10.1149/2.0441414jes>.
- [29] S. Doubaji, M. Valvo, I. Saadoune, M. Dahbi, K. Edström, Synthesis and characterization of a new layered cathode material for sodium ion batteries, *J. Power Sources.* 266 (2014) 275.
- [30] G. J. Owens, R. K. Singh, F. Foroutan, M. Alqaysi, C.-M. Han, C. Mahapatra, H.-W. Kim, J. C. Knowles, Sol–gel based materials for biomedical applications, *Prog. Mater. Sci.* 77 (2016) 1.
- [31] A. E. Danks, S. R. Hall, Z. Schnepf, The evolution of “sol-gel” chemistry as a technique for materials synthesis, *Mater. Horizons.* 3 (2016) 91.
- [32] X. C. Jiang, C. Y. Chen, W. M. Chen, A. B. Yu, Role of Citric Acid in the Formation of Silver Nanoplates through a Synergistic Reduction Approach, *Langmuir.* 26 (2010)

4400.

- [33] M. Tella, G. S. Pokrovski, Stability and structure of pentavalent antimony complexes with aqueous organic ligands, *Chem. Geol.* 292–293 (2012) 57.
- [34] Y. Jiang, S. Yang, Z. Hua, H. Huang, Sol-gel autocombustion synthesis of metals and metal alloys, *Angew. Chemie - Int. Ed.* 48 (2009) 8529.
- [35] W. Morales, M. Cason, O. Aina, N. R. de Tacconi, K. Rajeshwar, Combustion Synthesis and Characterization of Nanocrystalline WO₃, *J. Am. Chem. Soc.* 130 (2008) 6318.
- [36] A. Varma, A. S. Mukasyan, K. T. Deshpande, P. Pranda, P. R. Erri, Combustion Synthesis of Nanoscale Oxide Powders: Mechanism, Characterization and Properties, *MRS Proc.* 800 (2003) 1.
- [37] C. Sole, N. E. Drewett, L. J. Hardwick, In situ Raman study of lithium-ion intercalation into microcrystalline graphite, *Faraday Discuss.* 172 (2014) 223.
- [38] C. Sole, N. E. Drewett, F. Liu, A. M. Abdelkader, I. A. Kinloch, L. J. Hardwick, The role of re-aggregation on the performance of electrochemically exfoliated many-layer graphene for Li-ion batteries, *J. Electroanal. Chem.* 753 (2014).
- [39] J. Zou, C. Sole, N. E. Drewett, M. Velický, L. J. Hardwick, In Situ Study of Li Intercalation into Highly Crystalline Graphitic Flakes of Varying Thicknesses, *J. Phys. Chem. Lett.* 7 (2016) 4291.
- [40] C. Y. Xu, P. X. Zhang, L. Yan, Blue shift of Raman peak from coated TiO₂ nanoparticles, *J. Raman Spectrosc.* 32 (2001) 862.

- [41] M. Gaberscek, R. Dominko, M. Bele, M. Remskar, D. Hanzel, J. Jamnik, Porous, carbon-decorated LiFePO_4 prepared by sol–gel method based on citric acid, *Solid State Ionics*. 176 (2005) 1801.
- [42] C. Xia, C. Nian, Z. Huang, Y. Lin, D. Wang, C. Zhang, One-step synthesis of carbon-coated $\text{Li}_4\text{Ti}_4.95\text{Nd}_{0.05}\text{O}_{12}$ by modified citric acid sol–gel method for lithium-ion battery, *J. Sol-Gel Sci. Technol.* 75 (2015) 38.
- [43] K. Wang, Z. Yin, P. Zhao, Synthesis of macroporous Li_4SiO_4 via a citric acid-based sol–gel route coupled with carbon coating and its CO_2 chemisorption properties, *Ceram. Int.* 42 (2016) 2990.
- [44] X. Liu, Y. Du, X. Xu, X. Zhou, Z. Dai, J. Bao, Enhancing the Anode Performance of Antimony through Nitrogen-Doped Carbon and Carbon Nanotubes, *J. Phys. Chem. C*. 120 (2016) 3214.
- [45] L. Hu, X. Zhu, Y. Du, Y. Li, X. Zhou, J. Bao, A Chemically Coupled Antimony/Multilayer Graphene Hybrid as a High-Performance Anode for Sodium-Ion Batteries, *Chem. Mater.* 27 (2015) 8138.
- [46] D. Y. W. Yu, S. K. Batabyal, J. Gun, S. Sladkevich, A. A. Mikhaylov, A. G. Medvedev, V. M. Novotortsev, O. Lev, P. V. Prikhodchenko, Antimony and antimony oxide@graphene oxide obtained by the peroxide route as anodes for lithium-ion batteries, *Main Gr. Met. Chem.* 38 (2015) 43.
- [47] N. Zhang, Y. Liu, Y. Lu, X. Han, F. Cheng, J. Chen, Spherical nano-Sb@C composite as a high-rate and ultra-stable anode material for sodium-ion batteries, *Nano Res.* 8 (2015) 3384.

- [48] J. Wang, I. D. Raistrick, R. A. Huggins, Behavior of Some Binary Lithium Alloys as Negative Electrodes in Organic Solvent- Based Electrolytes, *J. Electrochem. Soc.* . 133 (1986) 457. <http://jes.ecsdl.org/content/133/3/457.abstract>.
- [49] K. C. Hewitt, L. Y. Beaulieu, J. R. Dahn, Electrochemistry of InSb as a Li Insertion Host: Problems and Prospects, *J. Electrochem. Soc.* 148 (2001) A402.
- [50] L. Baggetto, H.-Y. Hah, J.-C. Jumas, C. E. Johnson, J. A. Johnson, J. K. Keum, C. A. Bridges, G. M. Veith, The reaction mechanism of SnSb and Sb thin film anodes for Na-ion batteries studied by X-ray diffraction, ^{119}Sn and ^{121}Sb Mössbauer spectroscopies, *J. Power Sources.* 267 (2014) 329.
- [51] P. K. Allan, J. M. Griffin, A. Darwiche, O. J. Borkiewicz, K. M. Wiaderek, K. W. Chapman, A. J. Morris, P. J. Chupas, L. Monconduit, C. P. Grey, Tracking Sodium-Antimonide Phase Transformations in Sodium-Ion Anodes: Insights from Operando Pair Distribution Function Analysis and Solid-State NMR Spectroscopy, *J. Am. Chem. Soc.* 138 (2016) 2352.
- [52] O. Degtyareva, V. V Struzhkin, R. J. Hemley, High-pressure Raman spectroscopy of antimony: As-type, incommensurate host-guest, and bcc phases, *Solid State Commun.* 141 (2007) 164.
- [53] M. B. Tzolov, M. N. Iliev, Raman scattering from monoalkali (Na-Sb and K-Sb), bialkali (Na-K-Sb) and multialkali (Na-K-Sb-Cs) photocathodes, *Thin Solid Films.* 213 (1992) 99.
- [54] L. J. Hardwick, P. W. Ruch, M. Hahn, W. Scheifele, R. Kötz, P. Novák, In situ Raman spectroscopy of insertion electrodes for lithium-ion batteries and supercapacitors: First cycle effects, *J. Phys. Chem. Solids.* 69 (2008) 1232.



Scheme 1. Schematic diagram of sol-gel synthesis.

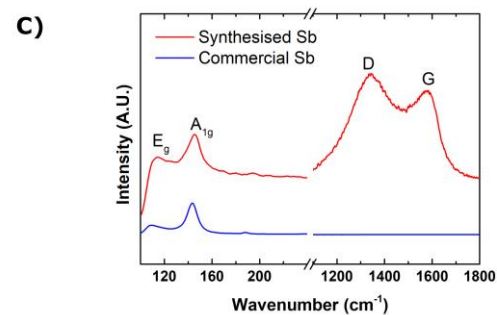
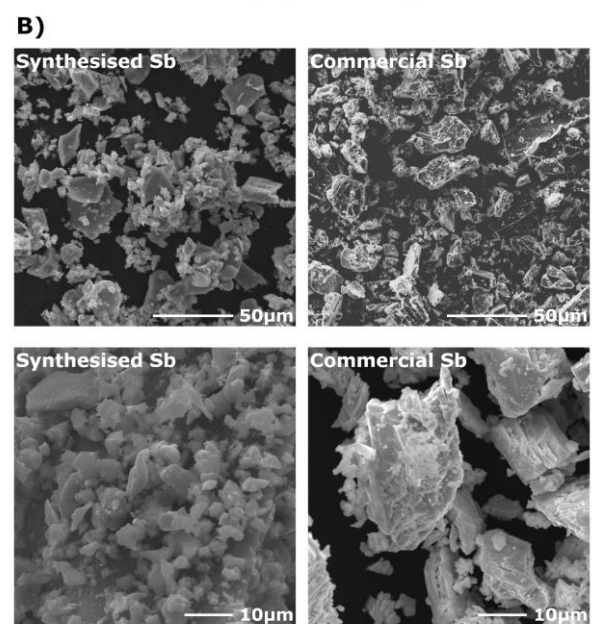
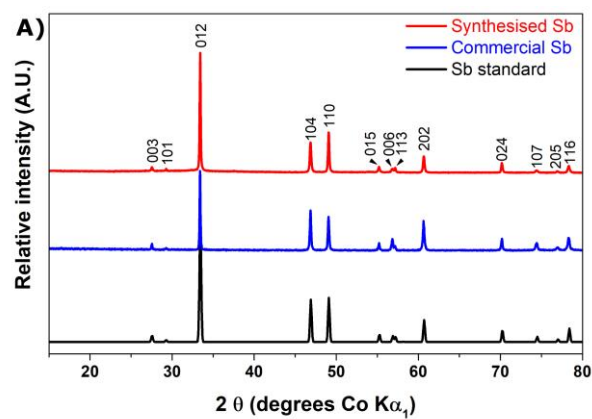


Figure 1. A) PXR D patterns for **sol-gel synthesised**, **commercial** and ICSD standard antimony.

B) Scanning electron microscope (SEM) images of the sol-gel synthesised and commercial antimony.

C) Raman spectra of the **sol-gel synthesised** and **commercial** antimony.

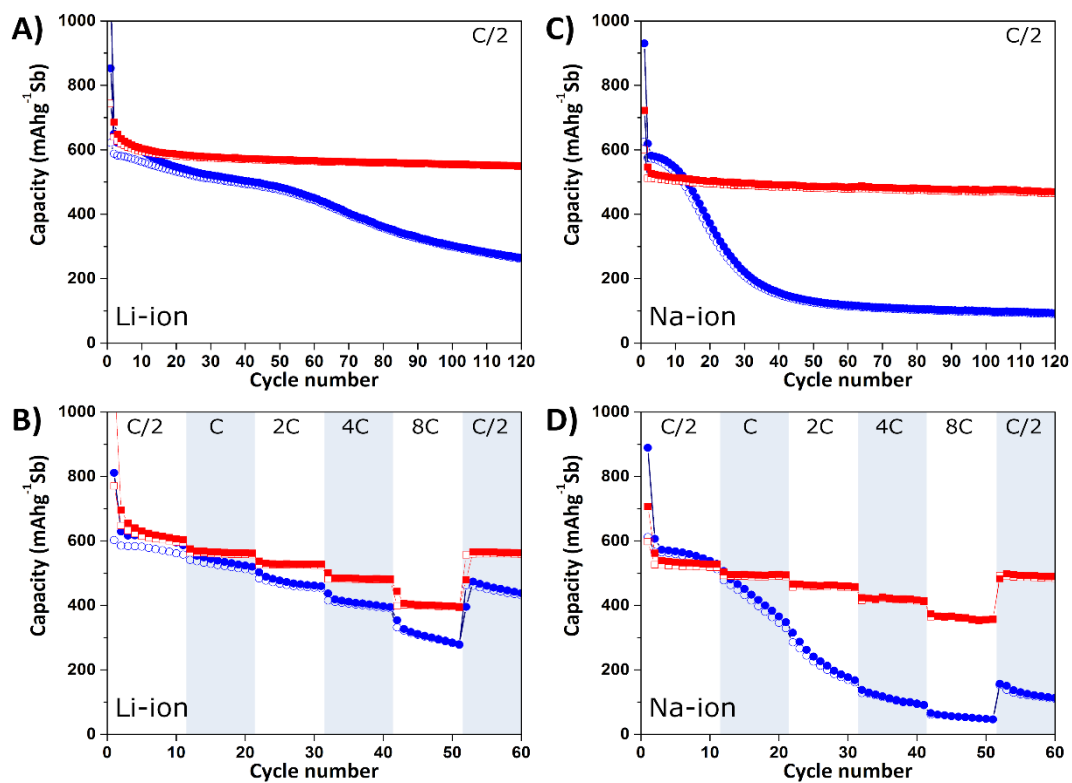


Figure 2. The cyclability and rate capability plots of sol-gel synthesised and commercial antimony vs. lithium (A and B respectively) and vs. sodium (C and D respectively). 1C is taken as being 660 mAgh⁻¹Sb, based on the theoretical capacity of antimony.

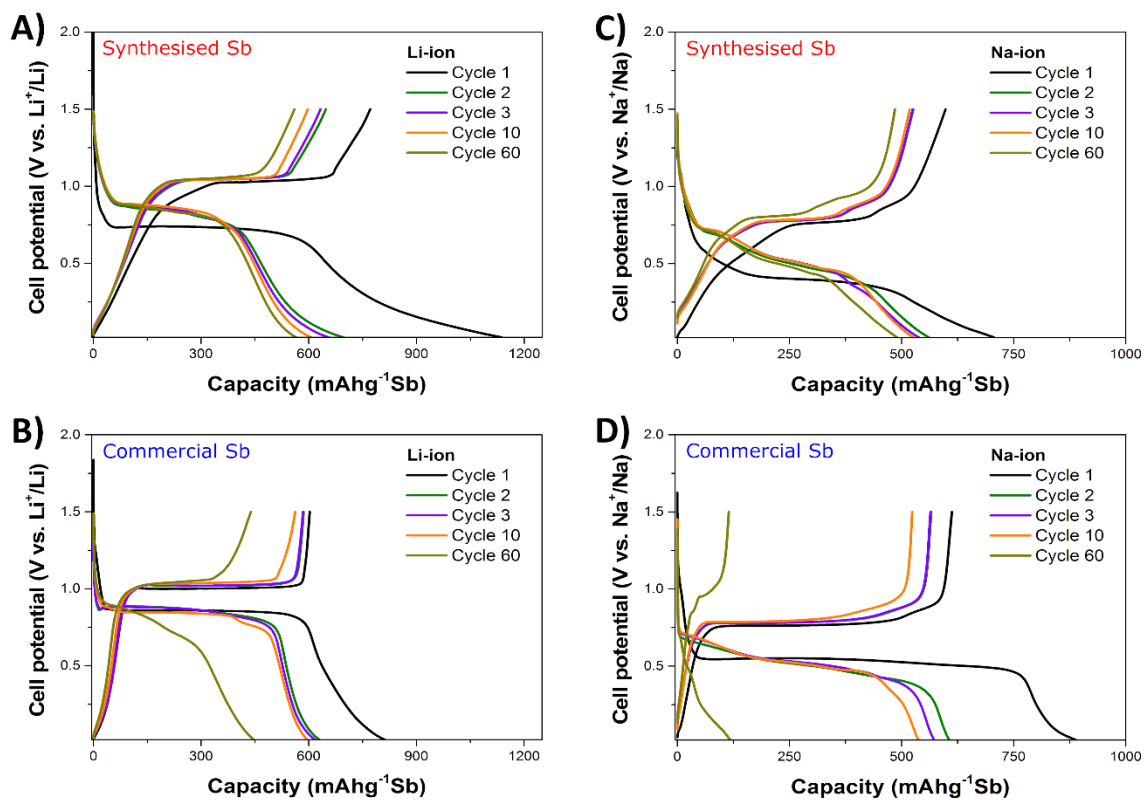


Figure 3. The load curves of sol-gel synthesised and commercial antimony at C/2 rate vs. lithium (A and B respectively) and vs. sodium (C and D respectively).

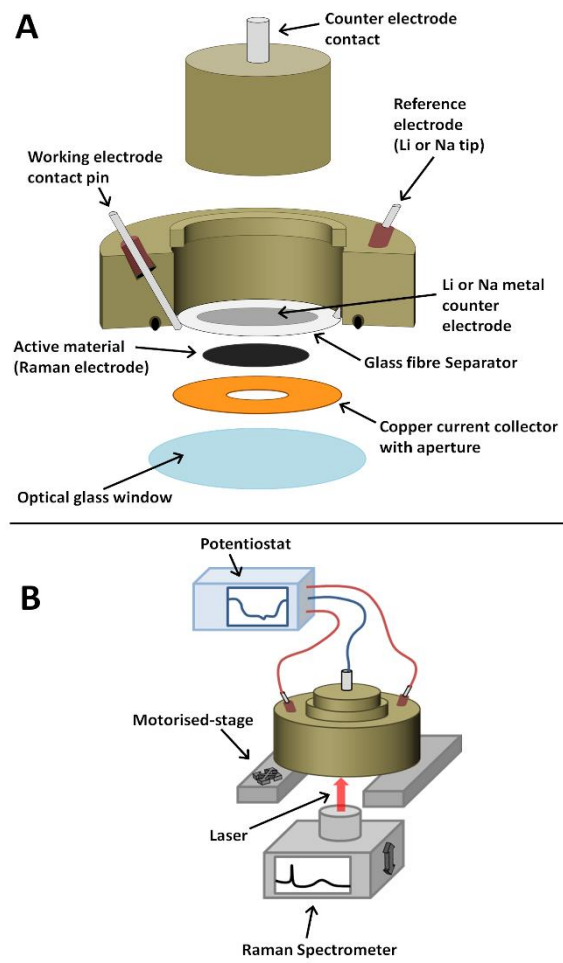


Figure 4. Schematic of Raman cell setup.

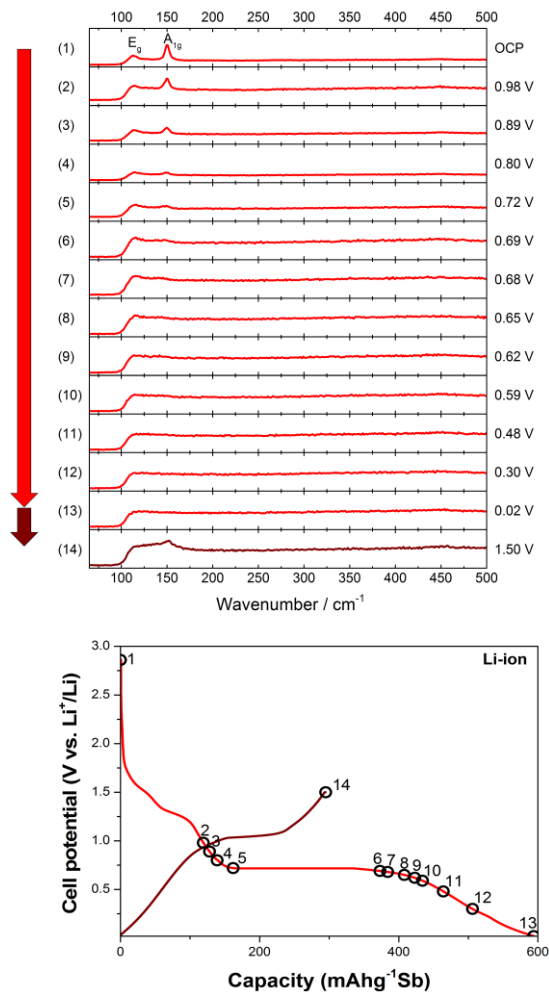


Figure 5. *In situ* Raman spectroscopy data of sol gel synthesised antimony vs. lithium over 1 charge/discharge cycle at $60\mu\text{A g}^{-1}$.

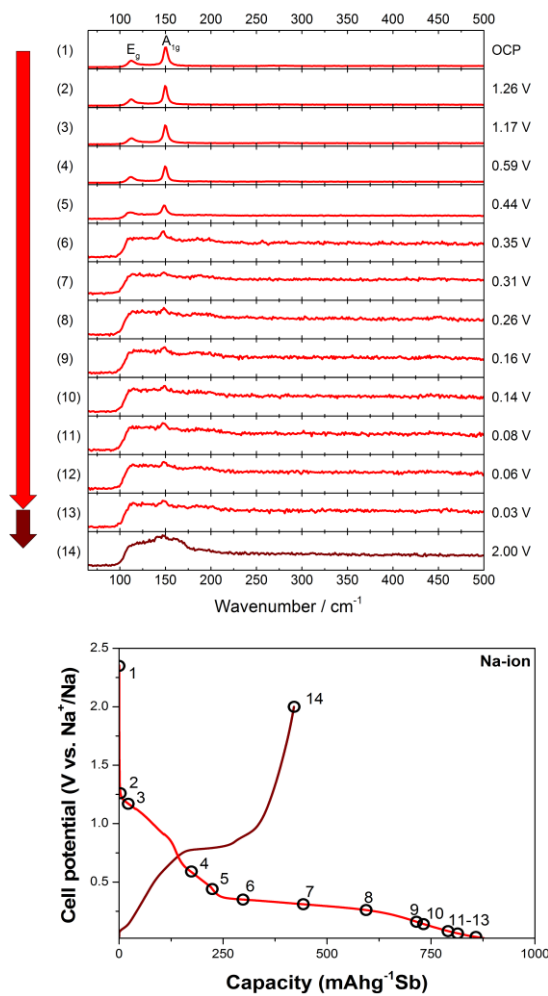


Figure 6. *In situ* Raman spectroscopy data for sol-gel synthesised antimony vs. sodium over 1 charge/discharge cycle at $60\mu\text{A g}^{-1}$.